Analog Integrated Circuits and Signal Processing
https://doi.org/10.1007/s10470-023-02210-7

Design and modeling of film bulk acoustic resonator considering temperature compensation for 5G communication

Xiushan Wu[1] · Lin Xu[2] · Ge Shi[2] · Xiaowei Zhou[2] · Jianping Cai[1]

Received: 22 December 2022 / Revised: 13 March 2023 / Accepted: 17 November 2023

Abstract
The new generation of communication systems requires radio frequency (RF) filters with better performance indicators, and traditional RF filters can no longer satisfy the requirements of increasingly sophisticated wireless communication equipment. Piezoelectric Film bulk acoustic resonators (FBARs) have gradually become a focus of communication system research. In this study, the temperature effect was considered in the FBAR electrical model. SiO_2 with a positive temperature coefficient was placed under the bottom electrode to perform temperature compensation. COMSOL software was used to study the shape of the electrode of the FBAR unit, the irregular shape of the electrode could obtain a smoother resonant frequency curve, and the common cavity and back erosion structure of the FBAR unit were studied, to extract the corresponding dielectric loss and mechanical loss of the piezoelectric layer, and to optimize the one-dimensional electrical model further. The optimized electrical model was used to design an FBAR filter. The center frequency was 3.52 GHz, the bandwidth was 115 MHz, the insertion loss was 0.87 dB, the in-band ripple was 1.32 dB, the out-of-band rejection was better than − 40 dB, and the absolute value of temperature coefficient of frequency was 7.09 ppm/°C, basically achieving the expected performance, which can be applied to the design of RF filters in mobile phones and other wireless terminals where the temperature requirement is harsh, and provides a solution for frequency selection and control in the field of high frequency communication.

Keywords Film bulk acoustic resonator (FBAR) · Filter · Insertion loss · Temperature coefficient of frequency (TCF)

1 Introduction

With the development of science and technology, the development of mobile communication devices has accelerated, and they have widely penetrated all aspects of society. To meet the communication needs, the mobile communication industry is constantly improving communication technology. It has undergone changes from 2G to today's 5G, but 4G networks are still dominant. For the current 5G system, there are still problems that need to be solved urgently in terms of operating frequency, loss and temperature drift. The RF front end is an important part of the communication system. In the global sales distribution of RF front ends, the filter accounts for the largest share [1]. In general, the development of RF filters directly affects the development of the communication industry, Therefore, it is imperative to find a filter with high-temperature, stability, low insertion loss, and integration. Compared with existing RF filters, FBAR filters have significant advantages, such as a high operating frequency, low insertion loss, high quality factor, high effective electromechanical coupling coefficient, and high stability. They can be integrated with CMOS [2–6] and great prospects in the field of mobile communications, in the global RF front-end sales distribution, the filter accounts for the largest amount, the market scale reached 8 billion dollars in 2017, and is predicted to reach 22.5 billion dollars in 2023, so the FBAR filter will have a broader application prospect.

Many enterprises, scientific research institutes, and universities worldwide have participated in research on FBAR devices. For the study of a single FBAR, Newell [7] developed the first Bragg reflector resonator with a resonant frequency of 2–7 MHz in 1965. That was the beginning of research on FBAR devices. Kumar [8], Nor Ni [9], Kadota [10], and others have studied the loss factor, performance analysis, process parameters, and other aspects of FBARs.

✉ Xiushan Wu
wuxs@zjweu.edu.cn

[1] The College of Electrical Engineering, Zhejiang University of Water Resources and Electric Power, Hangzhou, China

[2] The College of Mechanical and Electrical Engineering, China Jiliang University, Hangzhou, China

Published online: 21 December 2023

The temperature compensation and test characterization of FBARs have been studied by Nishihara [11], Igeta [12], Morales [13], and others. For the FBAR filter research process, Li [14] produced a filter with a center frequency of 5.5 GHz. Zou [15] proposed a dual-mode FBAR-based RF dual-frequency filter in 2020. Su et al. [16] proposed a filter with a 15°YX-lithium niobate/silicon dioxide/silicon multilayer structure. In research on FBARs. Since there will be shear waves in the working process of FBAR, some parasitic resonance will be caused, which will affect the in-band performance of FBAR filter, such as insertion loss, etc., researchers eliminate stray mode and high harmonic mode by optimizing the effective region of FBAR [17]. The displacement and strain energy limits in the middle of the resonator are realized by designing an asymmetric FBAR [18]. The further study of temperature compensation, insertion loss, and processing technology is needed. To date, research on the optimization of the temperature effect and insertion loss of FBAR filters is lacking. If the TCF value of the device is too large, it will be deeply affected by temperature, affect the working frequency, and eventually seriously deteriorate the noise coefficient and other performance of the RF front end. If the insertion loss of the device is too large, the working efficiency of the device will be affected. Therefore, it is necessary to design a high performance FBAR filter.

In this work, an AlN-based FBAR filter was designed. It works at communication frequencies of 3.40–3.60 GHz, and the temperature effect and loss parameters related to the piezoelectric layer (PE) are added to the electrical model of the FBAR unit. An FBAR filter with low TCF value and good in-band and out-of-band performance was fabricated, the center frequency was 3.52 GHz, the bandwidth was 115 MHz, the insertion loss was 0.87 dB, the in-band ripple was 1.32 dB, the out-of-band rejection was better than − 40 dB, and the absolute value of temperature coefficient of frequency was 7.09 ppm/°C. It is more suitable for high frequency applications where the temperature requirement is harsh.

2 Theoretical analysis and research on improvement of electrical impedance model

2.1 Theoretical analysis

The operation of a FBAR is based on the piezoelectric material of the PE. When an RF alternating voltage is applied to the device through the electrode layer, the inverse piezoelectric effect causes the device to produce a mechanical expansion and contraction motion with the change in the electric field and then generate vibration [19]. The vibration of the piezoelectric film layer excites the bulk acoustic wave propagating along the longitudinal direction of the film. The FBAR generates multiple sets of resonance states during operation, and generally only the fundamental frequency resonance (n = 0) is considered [20]. In each resonance group, there are the series resonant frequency f_s and parallel resonance frequency f_p, as shown in Fig. 1.

The effective electromechanical coupling coefficient k_{eff}^2 [21] and the quality factor Q value [22] are important indicators to measure the performance of FBAR devices, and k_{eff}^2 is used to characterize the conversion efficiency of electrical and mechanical energy in the resonator, f_s is the series resonant frequency and f_p is the parallel resonant frequency. The quality factor is used to characterize the ratio of the energy that can be stored by a resonant device or a tank circuit to the energy lost in one cycle, $\frac{d\varphi_z}{df}$ represents the derivative of the impedance phase of the resonator with respect to the frequency. The calculation of the two indicators is,

$$K_{eff}^2 = \frac{\pi^2}{4}\left(\frac{f_p - f_s}{f_p}\right) \tag{1}$$

$$Q = Q_{s/p} = \frac{f_{s/p}}{2}\left|\frac{d\varphi_z}{df}\right|_{f_{s/p}} \tag{2}$$

2.2 Improvement of electrical impedance model

The transmission characteristics of plane acoustic waves in ordinary elastic films and piezoelectric films in FBARs can be deduced according to the theory of the sound field in solids [23]. Based on this, the electrical impedance expression of an FBAR can be obtained, and the electrical impedance of

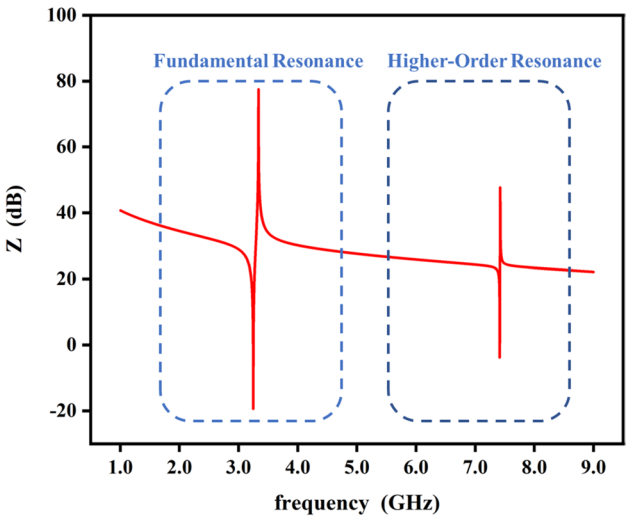

Fig. 1 Resonance state of the FBAR unit

the FBAR unit can be obtained by simplification. The model cannot simulate the temperature effect of the device. In the actual operation of the resonator, the temperature effect is inevitable, so it is necessary to establish a model considering it.

When FBAR works, each film layer is affected by the external ambient temperature and the heat generated by the internal work. According to the frequency calculation formula of the FBAR under ideal conditions [23],

$$f = (n+1)\frac{v}{d}, (n = 0, 1, 2, \ldots) \tag{3}$$

where n is the resonant state, v is the longitudinal sound velocity of the device, and d is the thickness of the resonator. Therefore, the effect of temperature on the longitudinal acoustic wave velocity of the material and the thickness of the material should be considered. The speed of sound (v) of the material can be expressed as a function of the elastic constant (c) and density (ρ) of the material,

$$v = f(c, \rho) = \sqrt{\frac{c_{33}^{D}}{\rho}} \tag{4}$$

The relationship between the density $\rho(T)$ of the material and the outside temperature is,

$$\rho(T) = \rho(T_0)(1 - (\alpha_{11} + \alpha_{22} + \alpha_{33})\Delta T) \tag{5}$$

In Eq. (5), α_{11}, α_{22}, and α_{33} are the thermal expansion coefficients along the direction of sound propagation and two directions perpendicular to the sound wave, respectively. In the equation, 10^{-6} is the order of magnitude of the coefficient of thermal expansion, and the value of $(1-(\alpha_{11}+\alpha_{22}+\alpha_{33})\Delta T)$ is approximately 1, so the density of the material can be ignored.

In Eq. (4), c_{33}^{D} represents the stiffness matrix of piezoelectric materials in the z-direction. "Stiffness" refers to the ability of a material to resist deformation when subjected to force and is often used to characterize the ease of elastic deformation of a material or structure. The law of the stiffness matrix in the z-direction of the material changing with temperature can be expressed by,

$$c^{D}(\Delta T) = c^{D}(1 + 2 \times TCF_x \times \Delta T) \tag{6}$$

where TCF_x is the temperature coefficient of frequency of the material, and the average rate of change of the natural frequency of the FBAR device when the temperature changes by 1 °C [24] is,

$$TCF = \frac{1}{f}\frac{df}{dT} = \frac{1}{v}\frac{dv}{dT} - \frac{1}{\lambda}\frac{d\lambda}{dT} \tag{7}$$

where λ represents the acoustic wavelength, and f represents the frequency.

By combining Eqs. (4) and (6), the relationship between the longitudinal sound speed and temperature change in material x can be obtained,

$$v\_x(\Delta T) = v\_x \times \sqrt{1 + 2 \times TCF_x \times \Delta T} \tag{8}$$

At the same time, acoustic impedance (Z) of the material is related to the density of the material and the speed of sound,

$$Z = \rho \cdot v_x(\Delta T) \tag{9}$$

As the temperature changes, the density of the material is considered to remain constant, so the acoustic impedance is mainly determined by the sound speed of the material,

$$Z = \rho \cdot v_x(\Delta T) = \rho \times v_x \times \sqrt{1 + 2 \times TCF_x \times \Delta T} \tag{10}$$

Because the sound velocity of a material is related to its elastic constant and density, Eq. (7) can be transformed into,

$$TCF = \frac{1}{2} \cdot \left(\frac{1}{c} \cdot \frac{\partial c}{\partial T} + \frac{1}{\rho} \cdot \frac{\partial \rho}{\partial T}\right) - \left(\frac{1}{\lambda} \cdot \frac{\partial \lambda}{\partial T}\right) \tag{11}$$

The wavelength can be represented by the thickness of the piezoelectric film ideally, and using ρ = M/V, one obtains,

$$TCF = \frac{1}{2} \cdot \left(\frac{1}{c} \cdot \frac{\partial c}{\partial T} + \frac{1}{V} \cdot \frac{\partial V}{\partial T}\right) - \left(\frac{1}{d} \cdot \frac{\partial d}{\partial T}\right) \tag{12}$$

where $\frac{1}{V} \cdot \frac{\partial V}{\partial T}$ and $\frac{1}{d} \cdot \frac{\partial d}{\partial T}$ can also be represented by the thermal expansion coefficient α as,

$$\frac{1}{V} \cdot \frac{\partial V}{\partial T} = -(\alpha_{11} + \alpha_{22} + \alpha_{33}) \tag{13}$$

$$\frac{1}{d} \cdot \frac{\partial d}{\partial T} = \alpha_{11} \tag{14}$$

Putting Eqs. (13) and (14) into Eq. (12),

$$TCF = \frac{1}{2} \cdot \left(\frac{1}{c} \cdot \frac{\partial c}{\partial T} - \alpha_{11} + \alpha_{22} + \alpha_{33}\right) \tag{15}$$

The thermal expansion coefficients are mainly divided into two categories, one is the bulk thermal expansion coefficient, and the other is the linear thermal expansion coefficient. Here, $\frac{1}{d} \cdot \frac{\partial d}{\partial T}$ is the expression for the coefficient of linear thermal expansion (αT). This part is eliminated in the process of substitution in the previous step, which also shows that the linear thermal expansion coefficient is not the main reason for the frequency drift of the device when the external temperature changes.

For the equivalent circuit of the existing electrical model, according to Eqs. (6), (8), and (10), the improved electrical impedance model is as shown in Fig. 2, where *eps* is the relative permittivity of the material, *alpha* represents the attenuation factor, v is the longitudinal sound velocity, Z represents

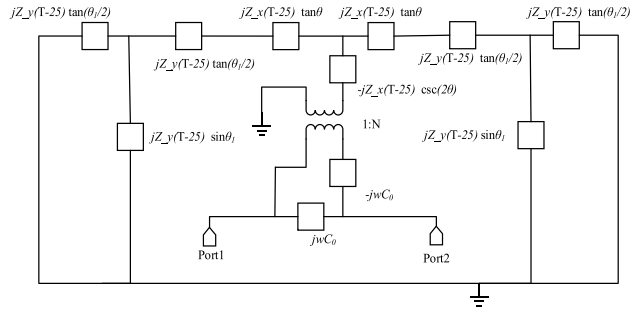

Fig. 2 Electrical model of considering temperature effects

the acoustic characteristic impedance, it has to do with the density of the material and the speed of sound, *thk* represents the film thickness, C_0 represents static capacitance, it is related to the relative permittivity of the material, the resonant area of the resonator and the thickness of the film. *Area* represents the area of the FBAR resonance area, *kt2* is the electromechanical coupling coefficient of the piezoelectric material. In the equivalent circuit, a transformer is used to replace the conversion of mechanical energy to electric energy of piezoelectric material, so N represents the number of turns of the transformer in the circuit *x* is the piezoelectric film layer material, and *y* represents the electrode layer or other acoustic layer material.

$$\begin{cases} \mathrm{C}_0 = \mathrm{eps}\_x \times \mathrm{Area}\_x/\mathrm{thk}\_x \\ N = \sqrt{2 \times \theta/(kt2\_x \times 2 \times \pi \times freq \times C_0 \times Z\_x)} \\ v\_i(T) = v\_i \times \sqrt{1 + 2 \times (TCF\_i) \times (T - 25)} \\ Z\_i(T) = \rho\_i \times v\_i(T) \\ \mathrm{k} = 2 \times \mathrm{pi} \times \mathrm{freq}/v\_i(T) \text{ - j} \times \mathrm{alpha}\_i/8.686 \\ \theta\_\mathrm{i} = k \times thk\_i/2 \\ \mathrm{eps}\_i \text{ ; thk}\_i \text{ ; alpha}\_i \end{cases} \quad (i = x, y) \tag{16}$$

3 Methods of temperature compensation

An FBAR is a negative frequency temperature coefficient device based on piezoelectric material, and the resonant frequency decreases with increasing temperature. The TCF value is not only related to Young's modulus but also to density, velocity, and the dielectric constant [25]. Adding a material with a positive temperature coefficient to the device compensates for the TCF value of the device. Because the frequency temperature coefficient of the FBAR piezoelectric material AlN designed in this study is − 25 ppm/°C, the frequency temperature coefficient of the electrode material metal Mo is − 60 ppm/°C [26]. The frequency temperature coefficient of SiO_2 is + 85 ppm/°C [27], which has great potential as a temperature compensation material for FBARs.

The temperature compensation layer based on SiO_2 can be placed between the bottom electrode (BE) and the support layer (SL), between the PE and the BE, and between the top electrode (TE) and the PE. When the thickness of the PE is 0.50 μm, the thickness of the electrode layer is 0.15 μm, the thickness of the SL is 0.20 μm, and the thickness of the temperature compensation layer is 0.10 μm. There are four cases for the location of SiO_2, and the results in Fig. 3 can be obtained. Moreover, the TCF of the four cases is calculated by Eq. (7), as shown in Table 1.

As shown in Fig. 3, when a 0.10-μm SiO_2 temperature compensation layer is added, the resonant frequency of the FBAR shows a decreasing trend compared with the case without the temperature compensation layer. This is because the temperature compensation layer has been added, increasing the transmission path of the acoustic wave inside the device while decreasing the frequency. If the thickness of each film layer remains unchanged, when the temperature compensation layer is placed near the PE, the frequency

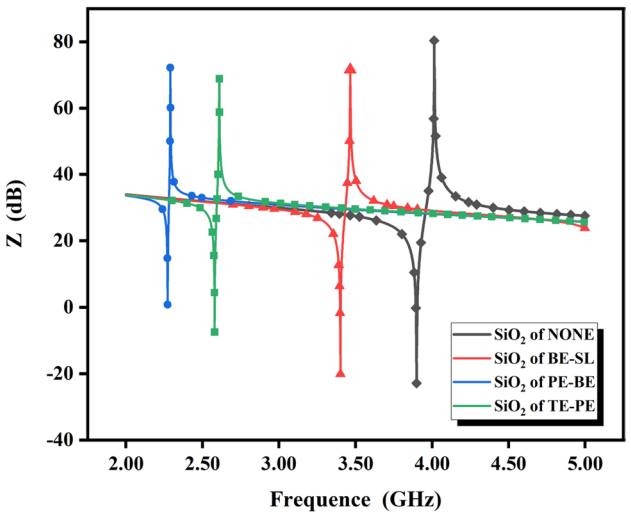

Fig. 3 Frequency characteristic curves of different temperature compensation layer positions

Table 1 TCF values of FBAR at different temperature compensation layer positions

Location of the temperature compensation layer	TCF (ppm/°C)
NONE	− 28.32
BE-SL	− 25.39
PE-BE	23.57
TE-PE	6.79

of the resonator has the most significant impact. When a temperature compensation layer with the same thickness is placed far from the PE, the device is affected. The resonant frequency has relatively little effect. As shown in Fig. 3, when a 0.10-μm SiO_2 temperature compensation layer is added, the resonant frequency of the FBAR shows a decreasing trend compared with the case without the temperature compensation layer. This is because the temperature compensation layer has been added, increasing the transmission path of the acoustic wave inside the device while decreasing the frequency. If the thickness of each film layer remains unchanged, when the temperature compensation layer is placed near the PE, the frequency of the resonator has the most significant impact. When a temperature compensation layer with the same thickness is placed far from the PE, the device is affected. The resonant frequency has relatively little effect. The attenuation coefficient of SiO_2 layer is large, reaching 1040 dB/m, while that of AlN and Mo are 800 dB/m and 500 dB/m respectively. Therefore, if SiO_2 layer is set on both sides of the piezoelectric layer, there will be more acoustic loss in this layer. Therefore, when the SiO_2 layer is set between the piezoelectric layer and the electrode layer, the resonant frequency is greatly reduced. Combined with the data in Table 1, when the temperature compensation layer is added between the PE and the TE, the temperature compensation of the device can be most effectively performed, and the TCF value is only 6.79 ppm/°C. The positive TCF of the SiO_2 layer contributes to the PE (AlN) and the electrode layer (Mo), and the overall TCF of the FBAR device gradually increases in the positive direction.

However, the following three situations should be considered. First, the resonant frequency in this research must be greater than 3.40 GHz. Second, it is considered that the SiO_2 film has a larger film stress than other film materials in the device. Third, the poor lattice matching of SiO_2 and AlN must be considered. To address these factors comprehensively, SiO_2 is arranged outside the Mo–AlN–Mo structure. The improvement of the structure is shown in Fig. 4. However, to achieve good frequency–temperature characteristics, the thickness of SiO_2 must be increased. Combined with the data in Table 1, when the temperature compensation layer is added between the PE and the TE, the temperature compensation of the device can be most effectively performed,

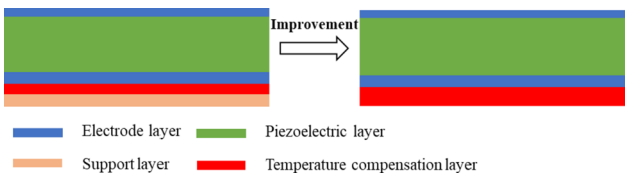

Fig. 4 Structure with temperature compensation layer added (without substrate)

and the TCF value is only 6.79 ppm/°C. The positive TCF of the SiO_2 layer contributes to the PE (AlN) and the electrode layer (Mo), and the overall TCF of the FBAR device gradually increases in the positive direction.

However, the following three situations should be considered. First, the resonant frequency in this research must be greater than 3.40 GHz. Second, it is considered that the SiO_2 film has a larger film stress than other film materials in the device. Third, the poor lattice matching of SiO_2 and AlN must be considered. To address these factors comprehensively, SiO_2 is arranged outside the Mo–AlN–Mo structure. The improvement of the structure is shown in Fig. 4. However, to achieve good frequency–temperature characteristics, the thickness of SiO_2 must be increased.

Through the above improved structure, the thickness of SiO_2 can be gradually increased to explore the variation rule of the TCF of FBARs. Therefore, the PE material is AlN, and its thickness is 0.50 μm. The electrode layer material is Mo, and the TE thickness is 0.15 μm. The thickness of the BE is 0.20 μm, the effective resonance area is 10,000 μm^2, and the thickness of the temperature compensation layer varies from 0.18 to 0.44 μm. Tests were performed in the temperature range of − 50 to 150 °C. The effect of the thickness variation of SiO_2 on the device, |TCF|, is shown in Fig. 5.

This analysis shows that, when the thickness of the PE is 0.50 μm, with the increase in the thickness of the temperature compensation layer, |TCF| shows a trend of first decreasing and then increasing. The negative frequency temperature coefficient of the layer still dominates, so the TCF at this time remains negative; however, when the thickness of the temperature compensation layer is 0.32–0.40 μm, the overall |TCF| of the device is less than 10 ppm/°C. When the thickness of the temperature compensation layer is approximately 0.37 μm, the TCF value of the device reaches 0. At

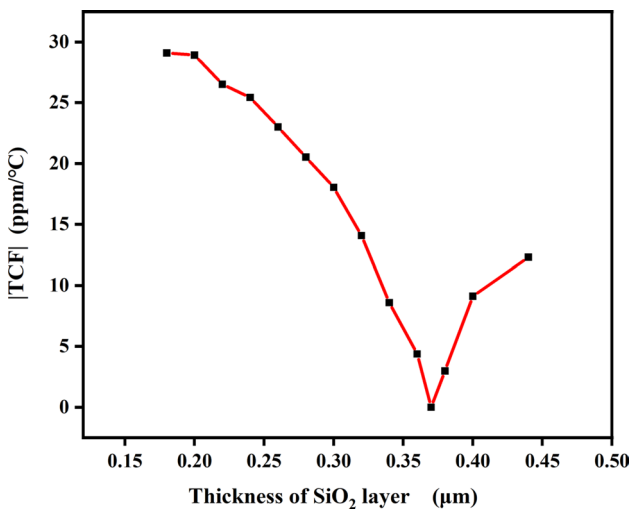

Fig. 5 Influence of SiO_2 layer thickness variation on |TCF|

this time, the thickness of the temperature compensation layer increases gradually. The positive frequency temperature coefficient of the temperature compensation layer plays a major role, and the TCF value at this time is positive. However, as the film thickness increases, the overall TCF of the device increases gradually, and the resonant frequency gradually deteriorates.

Considering the operating frequency and temperature compensation is convenient for filter design in the later stage. The materials and dimensions of the two FBARs are initially designed as shown in the Table 2. To meet the filter performance requirement in the later stage, the resonance area is adjusted, so only the setting range is given for the resonance area in Table 2.

4 Finite-element model establishment and research

4.1 Influence of different electrode shapes

The model obtained by electrical simulation can only be used to adjust the material of the FBAR and the thickness of each film and then analyze its resonant frequency. It cannot be used to analyze the size and vibration mode of the device [28]. An FBAR finite-element model based on COMSOL can make up for the deficiency of the electrical model.

In the process of electrical model simulation, the resonant area of the device affects its impedance value but not the resonant frequency, COMSOL can be used to build a three-dimensional (3D) model to study the effect of the electrode shape on the FBAR resonant characteristics when the resonant area has the same impact. Four electrode shapes (rectangle, circle, ellipse, and pentagon) are used.

The three-dimensional model of four electrode shapes was established in COMSOL. The material and thickness of the model were set according to Table 2, the electrostatic field was coupled with the solid mechanical field, and the free tetrahedral network was used for mesh division, as shown in Fig. 6. The model in Fig. 6 does not consider the substrate, because the focus of the experiment here is to study the shape of the electrode. The presence or absence of the substrate will not make a difference, but will increase the solution time. Finally, the frequency domain solver was selected for simulation, after the calculation is completed, create "Smith plotting Group" and then "Admittance plotting" in the result. Input "es.Y11" in the column of expression, and introduce the admittance value calculated by the device into it. The Smith impedance circle diagram here represents the input return loss of the FBAR. The Smith impedance diagram under four electrode shapes was obtained, as shown in Fig. 7.

Figure 7 shows that the Smith impedance charts of the rectangle and circle are not as smooth as those of the ellipse

Table 2 Structure parameters of series and parallel FBARs

Structure and materials		Parameters	
Structure	Materials	Series FBAR	Parallel FBAR
Top electrode	Mo	0.15 μm	0.15 μm
Piezoelectric layer	AlN	0.50 μm	0.50 μm
Bottom electrode	Mo	0.20 μm	0.23 μm
Temperature compensation (Support) layer	SiO_2	0.33 μm	
Resonant area	–	1×10^{-9}–2×10^{-8} μm^2	

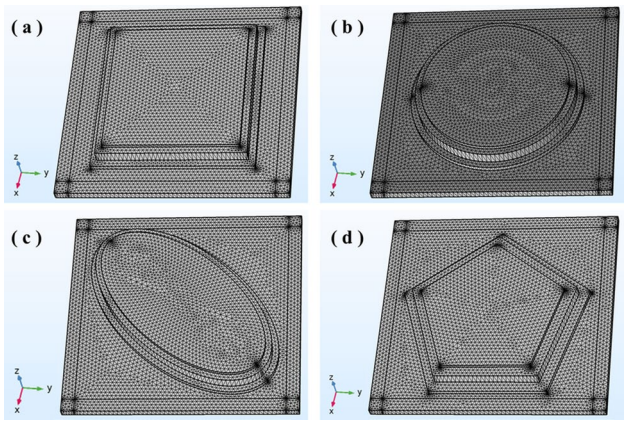

Fig. 6 Three-dimensional models of different electrode shapes: **a** rectangle, **b** circle, **c** ellipse, and **d** pentagon

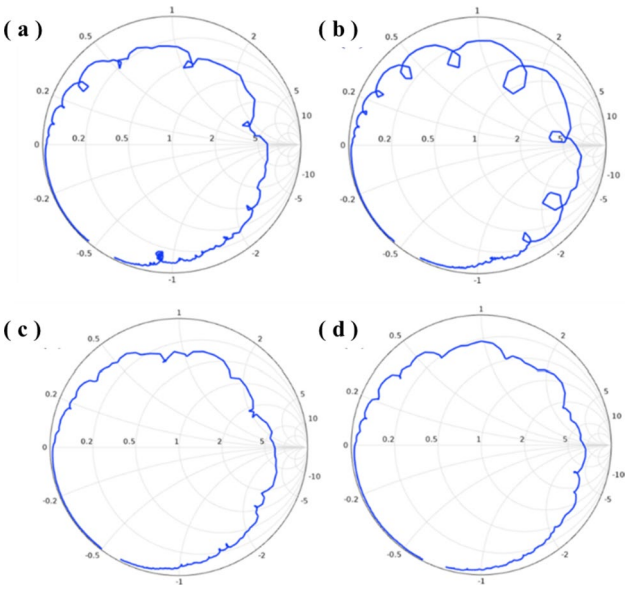

Fig. 7 Smith impedance diagram of FBAR with different electrode shapes: **a** rectangle, **b** circle, **c** ellipse, and **d** pentagon

and pentagon, and there are many small loops. The existence of the small circles indicates that electrode of these shapes generates parasitic resonance during operation.

The generation of the parasitic resonance occurs because, when the FBAR is working, in addition to generating longitudinal waves, it also excites transverse Lamb waves, while the elliptical and regular pentagons have nonparallel sides. The Lamb waves propagate to the electrode boundary, which changes the direction of reflection when reflected. Therefore, the irregular electrode shape reduces the possibility of forming spurious resonances by changing the reflection direction of the transverse Lamb waves.

Comparing Fig. 7c and d reveals that the elliptical electrodes still have parasitic resonances, and the pentagon Smith impedance diagram is smoother. Eliminating parasitic resonance as much as possible can significantly improve performance in the passband in the later stage of filter design. Therefore, in the later FBAR design process, the pentagon is used as the main shape.

4.2 Three-dimensional model establishment of FBAR unit

The models of the cavity type and the back-etched FBAR are established according to the parameters of each film layer of the series FBAR in Table 2 [29, 30]. The electrode shapes of both structures are regular pentagons. The thickness of the silicon substrate is 5 μm, the length is 210 μm, the width is 190 μm. The resonance area is 10,000 μm^2, and the cavity depth of the cavity-type structure is 2 μm, as shown in Fig. 8.

The combination of solid mechanics and the electrostatic field is used, ignoring the ohmic losses caused by the electrodes. Frequency domain research is employed for calculation in the frequency range of 3.10–3.80 GHz. The frequency sweep step size is set to 1 MHz for calculation and solution. The deformation displacement of the device can be obtained, and its impedance value can be obtained by the equation Z = log(abs(1/(es.Y11))). The frequency impedance characteristic curve of the device is thus drawn. The impedance amplitude, phase, and vibration displacement distribution of the FBAR unit of the two structures are shown in Fig. 9.

Figure 9 shows that the series resonant frequency $f_s = 3.47$ GHz and the parallel resonant frequency $f_p = 3.54$ GHz for the FBAR of the two structures. The effective electromechanical coupling coefficient is 5.09%. There are many parasitic resonances on the amplitude and phase curves of *Z* in Fig. 9, and the amplitudes and parasitic resonances on the phase correspond one to one. This is because the loss of the piezoelectric film layer is considered during the simulation process. The impedance amplitude diagrams of the two devices show that, between the series–parallel resonance frequencies of the cavity-type

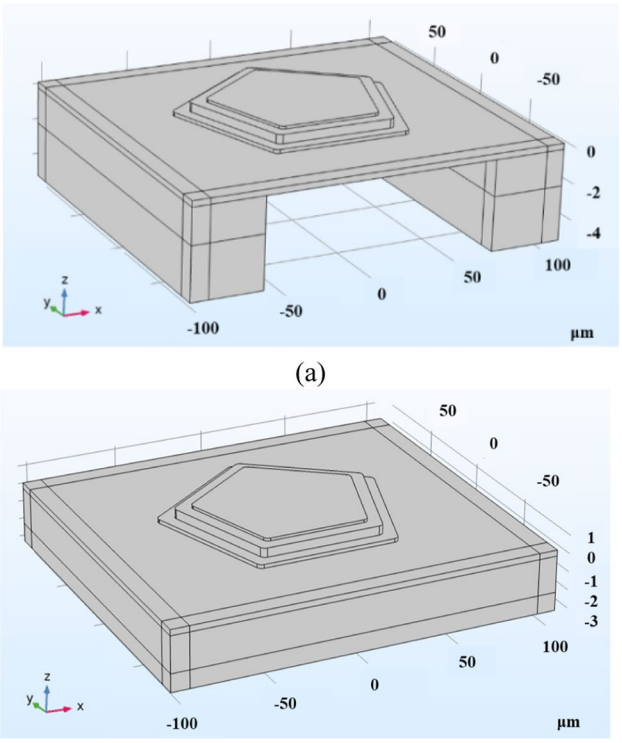

Fig. 8 Three-dimensional finite element models of the FBAR: **a** back-etched type and **b** cavity type

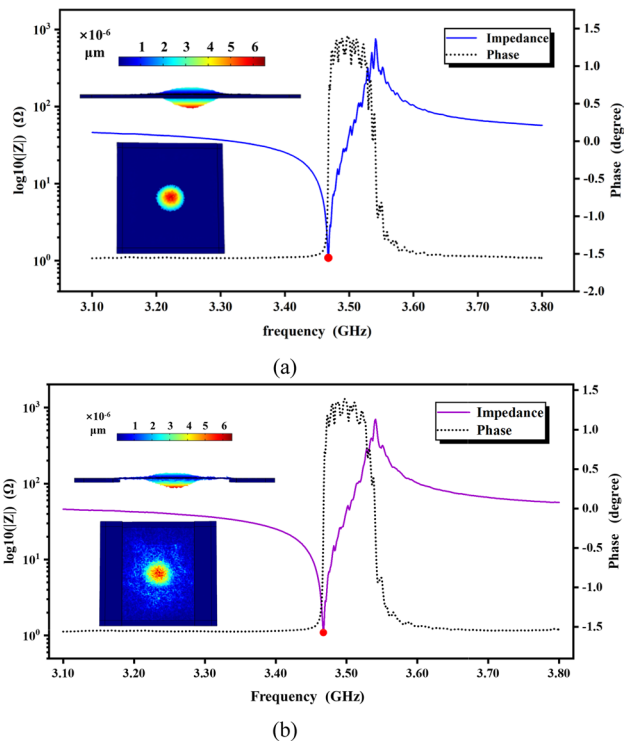

Fig. 9 Amplitude and phase of Z plotted: **a** cavity type FBAR and **b** back-etched FBAR

structure, the amplitude of the parasitic resonance that exists is more prominent, but the cavity-type structure is limited to a certain extent by the existence of the cavity structure. The transmission of sound waves is caused by the superposition of losses.

The maximum vibration displacement of the FBAR occurs at the series resonance frequency point — that is, the red point in Fig. 9. The figure shows the vibration displacement distribution of the FBAR device from the top and side views. The vibration displacement extends from the center position to the surrounding edge, and the vibration displacement gradually decreases. The maximum deformation displacement of the device occurs at a frequency of 3.47 GHz. The maximum vibrational displacement of the FBAR is within the deformation range of the piezoelectric material (AlN), indicating that the resonance characteristics generated by the designed FBAR are effective. Because the cavity-type structure can better confine the sound waves in the FBAR body, the distribution of its vibration displacement has a boundary.

4.3 Extraction of loss parameters

In order to design the filter accurately, the mechanical and dielectric losses of the piezoelectric film layer must be extracted and added to the one-dimensional electrical model.

Step 1: The static capacitance C_0 is extracted, and eight frequency points are taken at the far ends of the series and parallel resonance frequency points of the FBAR. The imaginary part Z_i of the impedance corresponding to each frequency point fi is found. The value of C_i at each frequency point is obtained separately, and the static capacitance C_0 is obtained by averaging C_i.

$$C_0 = \sum \frac{1}{2\pi f_i Z_i} = 1.01\text{p}F \tag{17}$$

Step 2: The dynamic capacitance is calculated according to the experimental results of the 3D model. The series resonance frequency f_s is 3.468 GHz, and the parallel resonance frequency f_p is 3.541 GHz.

$$C_m = \left((\frac{f_p}{f_s})^2 - 1 \right) \times C_0 = 0.043\text{p}F \tag{18}$$

Step 3: The dynamic inductance is calculated.

$$L_m = \frac{1}{(2\pi f_s)^2 \times C_m} = 49\text{n}H \tag{19}$$

Step 4: Quality factors Q_s and Q_p at the series and parallel resonance frequency points are employed. According to Eq. (2), one obtains $Q_s = 1054.45$ and $Q_p = 576.30$.

Step 5: The mechanical loss R_m of the piezoelectric film layer is obtained. In the COMSOL simulation, to consider the loss of electrodes and leads, $R_s = 0$. Combining L_m and Q_s, one obtains

$$R_m + R_s = \frac{2\pi f_s L_m}{Q_s} = 1.01\Omega \tag{20}$$

Step 6: The dielectric loss R_0 of the piezoelectric film layer can be obtained according to such parameters as Q_p and C_0:

$$R_0 = \frac{1}{2\pi f_p Q_p C_0} = 0.077\Omega \tag{21}$$

The mechanical loss and dielectric loss of the piezoelectric thin-film layer obtained through the above process further improves the electrical model of the FBAR. The PE part of the improved electrical model is shown in Fig. 10.

5 FBAR filters

A single FBAR unit has resonance characteristics but no filtering function. Multiple FBAR units are cascaded to a particular structure to achieve the required filtering function. The filter performance goals set in this research are a passband range of 3.40–3.60 GHz, bandwidth greater than 100 MHz, insertion loss and in-band ripple better than − 1.50 dB, out-of-band rejection better than − 40 dB, and device |TCF| less than 10 ppm/°C.

The common cascade structures are mainly L-type, T-type, and π-type. Based on the second-order L-type, the fourth-order, sixth-order, and seventh-order L-type structures were conducted, as shown in Fig. 11. Here, S_i (i = 1–7) represents the series FBAR unit, and P_j (j = 1–7) represents the parallel FBAR unit. The combination of a series FABR and a parallel FBAR unit is called a "first-order structure."

An analysis of the filter performance graph in Fig. 12 shows that, as the order increases from the second to the seventh, the in-band performance of the filter gradually deteriorates, and the insertion loss gradually increases. The in-band flatness also gradually deteriorates, and

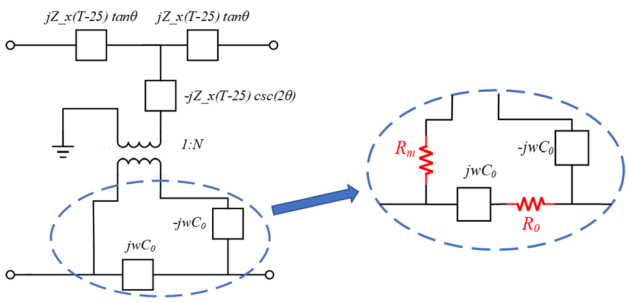

Fig. 10 Electrical model of the piezoelectric layer after adding the relevant losses

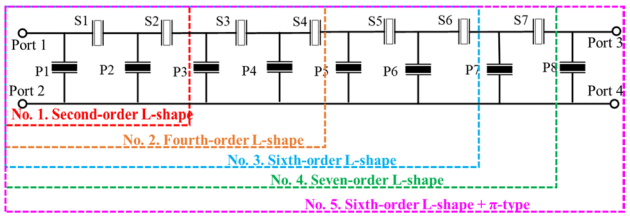

Fig. 11 FBAR filter structure

the passband width increases. It is reduced from 120 to 100 MHz; however, the out-of-band suppression capability of the filter is gradually enhanced. This is because of the gradual increase in the cascade order so that the filter has a signal shunting phenomenon outside the passband, improving the out-of-band performance of the filter. However, owing to internal losses in the FBAR unit, as the number of FBARs increases, the in-band performance of

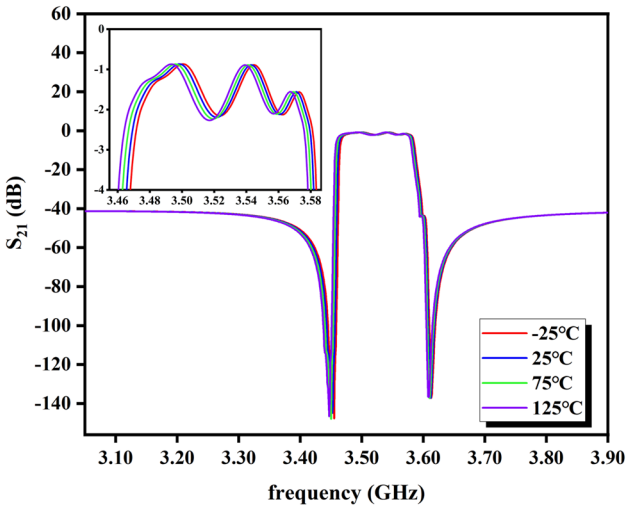

Fig. 13 S_{21} pictures of FBAR filter at different temperatures

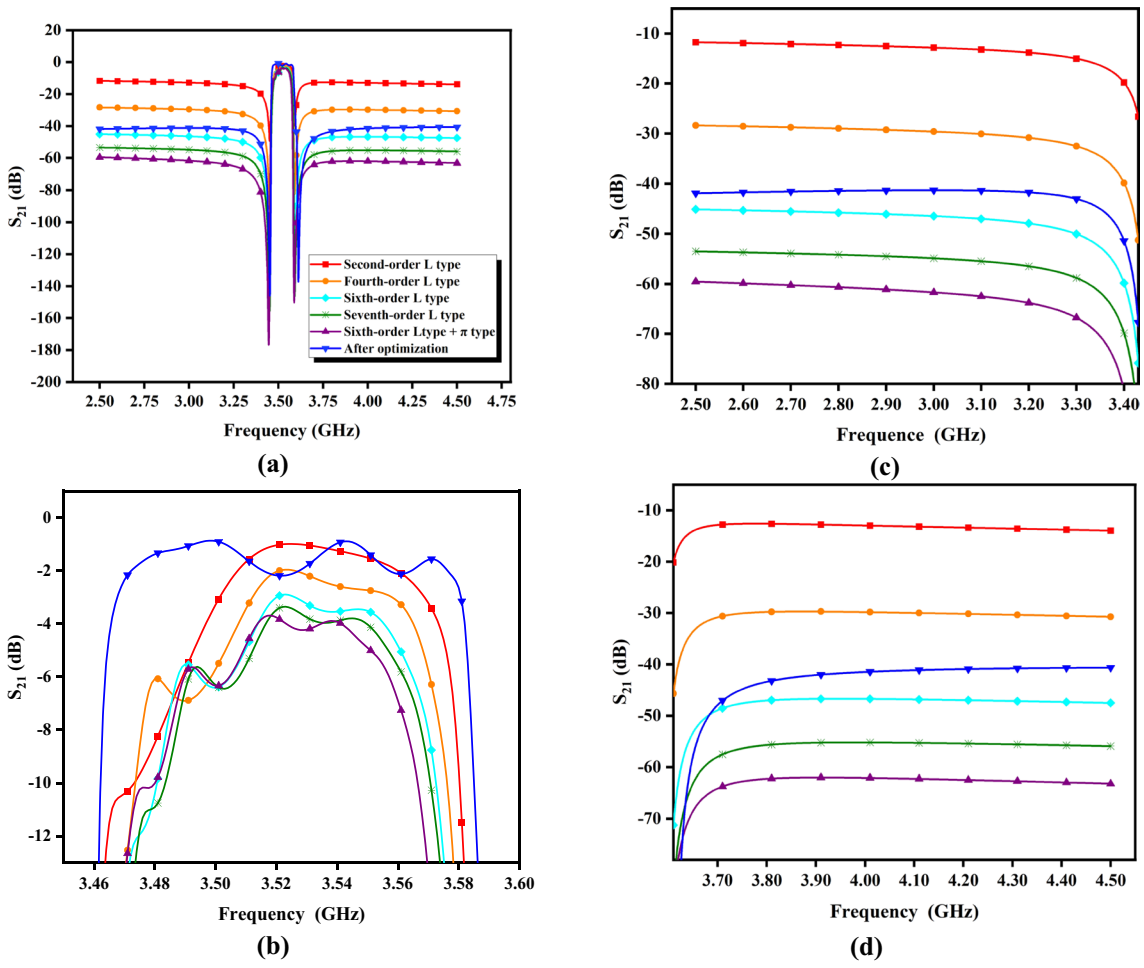

Fig. 12 Frequency response curves of FBAR filters of various structures: **a** full frequency band, **b** pass band, **c** left frequency band, and **d** right frequency band

Table 3 Performance index of the optimized FBAR filter and comparison with other research results

Performance index	[14]	[15]	[31]	[32]	[32, 33]	This work
Center frequency (GHz)	5.5	3.35	3.50	2.60	2.28	3.52
Bandwidth (MHz)	111	105	200	100	95	115
Insertion loss (dB)	−2.19	−2	−1.73	−2	≤2	−0.87
In-band ripple (dB)	>2	–	–	–	1.11	1.32
Out-of-band suppression (dB)	–	≤35	–	≤42	−40	≤41
|TCF| (ppm/°C)	–	–	–	–	11	7.09

the device deteriorates. Therefore, it is improved by the seventh-order structure.

Based on the seventh-order L-type structure, the first-order L-type structure is replaced by a π-type structure. The π-type structure has a better out-of-band suppression effect. The experimental results of this structure are shown in the purple line in Fig. 12. The loss is − 3.70 dB. The in-band ripple is 2.75 dB, the out-of-band rejection is ≤ 60 dB, and the |TCF| of the device is 11.07 ppm/°C.

The in-band performance of the filter does not meet the design requirements and must be optimized. The first optimization takes the resonance area as the optimization object, and the second optimization takes the thickness of the electrode layer as the optimization object. The filter response curve after optimization is shown by the blue line in Fig. 12.

The optimized filter was subjected to temperature experiments and tested at °25–125 °C. The S_{21} parameter curve of the obtained filter is shown in Fig. 13. According to Eq. (11), the TCF of the optimized filter can be obtained as 7.09 ppm/°C.

The performance index of the final FBAR filter and a comparison with the computer simulation results of other research results are shown in Table 3. The center frequency of the FBAR filter is in the range of 3.40–3.60 GHz, and the insertion loss is controlled within 1.50 dB. The 3-dB bandwidth reaches 115 MHz, the in-band ripple is controlled within less than 1.50 dB, and the out-of-band suppression of the filter is approximately − 41 dB.

6 Conclusion

In this study, an FBAR filter for the 5G communication frequency band is designed, and an electrical impedance model considering temperature effects is established. The SiO_2 layer with a positive temperature coefficient is placed under the BE to compensate the temperature of the FBAR unit. When the SiO_2 temperature compensation layer thickness is 0.32–0.40 μm, the overall |TCF| of the device is less than 10 ppm/°C. A finite-element simulation model is established, and the irregular (regular pentagon) electrode shape better suppress the parasitic resonance. The loss related to the piezoelectric thin-film layer is extracted from the finite-element model junction, and the one-dimensional electrical model is further optimized. The FBAR filter model is established by using the optimized one-dimensional electrical model. The optimized performance of the FBAR filter is as follows. The center frequency is 3.52 GHz, 3-dB bandwidth is 115 MHz, insertion loss is 0.867 dB, in-band ripple is 1.32 dB, out-of-band rejection is better than − 41 dB, and |TCF| is 7.09 ppm/°C, which provides a solution for frequency selection and control in the field of 5G communications, and is also suitable for high-frequency applications with demanding temperature requirements.

Author contributions XW Conceptalization, Formal analysis, Resources, Writing-Original Draft&Editing, Funding acquisition. LX Methodology, Formal analysis, Investigation, Data Curation, Writing-Original Draft. GS Resources, Investigation, Writing-Review. XZ Data Curation, Writing-Review JC Software, Validation, Project administration.

Funding This work was supported by the Natural Science Foundation of Zhejiang Province, China (Grant No. LY21F040001), which was obtained by Professor Wu Xiushan.

Data availability The data used to support the findings of this study are included within the article. The datasets generated and/or analyzed during the current study [due to ongoing research on the subject, not disclosed] are not publicly available but are available from the respective authors upon reasonable request.

Declarations

Conflict of interest The authors declare that they have no competing interest.

References

1. YOLE DEVELOPMENT. Industry Analysis: A large inventory of domestic RF chip companies [EB/OL]. http://www.yole.fr/, (2018).
2. Nor, N., Osman, R., Idris, M. S., et al. (2021). The influence of design parameters on the performance of FBAR in 10–14 GHz. INCAPE2017, 162, 1–5.
3. Campannell, H., Cabruja, E., Montserrat, J., et al. (2008). Thin-film bulk acoustic wave resonator floating above CMOS substrate. *IEEE Electron Device Letters, 29*(1), 28–30.

4. Hara, M., Yokoyama, T., Sakashita, T., et al. (2009). A study of the thin film bulk acoustic resonator filters in several ten GHz band. *IEEE Ultrasonics Symposium, 2*, 851–854.
5. Zhang, Y., Luo, J., Flewitt, A. J., et al. (2018). Film bulk acoustic resonators (FBARs) as biosensors: A review. *Biosensors and Bioelectronics, 116*, 1–15.
6. Krishnaswamy, S. V, Rosenbaum, J., Horwitz, S., et al. (1999). Film bulk acoustic wave resonator technology. In: *IEEE Symposium on Ultrasonics. IEEE*, 529–536.
7. Newell, W. E. (1965). Face-mounted piezoelectric resonators. *Proceedings of the IEEE, 53*(6), 575–581.
8. Kumar, Y., Rangra, K., Agarwal, R., et al. (2017). Design and simulation of FBAR for quality factor enhancement. *Mapan - Journal of Metrology Society of India, 32*(2), 113–119.
9. Nor NIM, Hasni AHM, Khalid N, et al. (2020). Carbon nanotube as electrode in film bulk acoustic wave resonator for improved performance. In*: 2nd International Conference on Applied Photonics and Electronics.* Putrajaya, MALAYSIA, 2203, 1–7.
10. Kadota, M., Ishii, Y., Tanaka, S., et al. (2021). A solidly mounted, high frequency, thickness shear mode bulk acoustic wave resonator using X-$LiTaO_3$ thin plate and SiO_2/Ta multilayer acoustic films. *Japanese Journal of Applied Physics, 60*(SD), SDDC11.
11. Noshihara, T., Taniguchi, S., Ueda, M., et al. (2015). Increased piezoelectric coupling factor in temperature-compensated film bulk acoustic resonators. *IUS, 2015*, 10–13.
12. Igeta, H., Totsuka, M., Suzuki, M., et al. (2018). Temperature characteristics of ScAlN/SiO_2 BAW resonators. In *IEEE International ultrasonics symposium, IUS*. 7–10.
13. Morales, R. Y. V., Cisneros, S. O., Perez, J. R. C., et al. (2021). 3D simulation-based acoustic wave resonator analysis and validation using novel finite element method software. *Sensors, 21*(8), 2715.
14. Li, L., Yiliang, Z., & Hongjun, L. (2019). A film bulk acoustic resonator filter for c band application. *Semiconductor technology, 44*(12), 951–955.
15. Zou, Y., Nian, L., Cai, Y., et al. (2020). Dual-mode thin film bulk acoustic wave resonator and filter. *Journal of Applied Physics*. https://doi.org/10.1063/50028702
16. Su, R., Shen, J., Lu, Z., et al. (2021). Wideband and low-loss surface acoustic wave filter based on 15°YX-$LiNbO_3$/SiO_2/Si structure. *IEEE Electron Device Letters, 42*(3), 438–441.
17. Pillai, G., Zope, A. A., Tsai, J. M. L., et al. (2017). Design and optimization of composite FBAR resonators. *IEEE Transactions on Ultrasonics, Ferroelectrics, and Frequency Control, 64*(12), 1864–1873.
18. Patel, R., Adhikari, M. S., & Boolchandani, D. (2020). Active area optimisation of film bulk acoustic resonator for improving performance parameters. *Electronics Letters, 56*(22), 1191–1194.
19. Liu, Y., Cai, Y., Zhang, Y., et al. (2020). Materials, design, and characteristics of bulk acoustic wave resonator: A review. *Micromachines, 11*(7), 1–26.
20. You, K., & Choi, H. (2020). Inter-stage output voltage amplitude improvement circuit integrated with class-b transmit voltage amplifier for mobile ultrasound machines. *Sensors, 20*, 6244.
21. Yang, Y. S., Lu, R. C., & Gong, S. B. (2020). High Q antisymmetric mode lithium niobate mems resonators with spurious mitigation. *IEEE Journal of Microelectromechanical Systems, 29*(2), 135–143.
22. Yi, X., Zhao, L., Ouyang, P., et al. (2022). High-quality film bulk acoustic resonators fabricated on AlN films grown by a new two-step method. *IEEE Electron Device Letters, IEEE, 43*(6), 942–945.
23. Yadira, R., Morales, V., Cissneros, S. O., et al. (2021). 3D simulation-based acoustic wave resonator analysis and validation using novel finite element method software. *Sensors, 21*(8), 1–18.
24. Wang, J. L., Park, M., Ansari, A., et al. (2022). High-temperature acoustic and electric characterization of ferroelectric Al0.7Sc0.3N Films. *IEEE Journal of Microelectromechanical Systems, 31*(2), 234–240.
25. Ahn, D., Jung, M., Ahn, S. E., et al. (2020). Compensation charge control and modeling for reproducing negative capacitance effect of hafnia ferroelectric thin films. *Advanced Materials Interfaces, 7*(23), 2001356.
26. Yanagirani, T., Kiuchi, M., Matsukawa, M., et al. (2006). Temperature characteristics of pure shear mode FBARs consisting of (11$\bar{2}$0) textured ZnO films, In: *Proceedings - IEEE Ultrasonics Symposium*, 1459–1462.
27. Jiang, S. Y., Jiang, P. Y., Liu, Y., Zhen, J. Y., et al. (2022). Research on low temperature drift thin film bulk acoustic resonator. *Piezoelectric and Acousto-Light, 44*(2), 171–174.
28. Xu, L., Wu, X., & Zeng, Y. (2021). Simulation and research of piezoelectric film bulk acoustic resonator based on mason model. *ICICM, 2021*, 184–188.
29. Liu, Y., Sun, K., Ma, J. Y., et al. (2021). Design and fabrication of temperature-compensated film bulk acoustic resonator filter based on the stress compensation effect. *Coatings, 12*(8), 1126.
30. Piazza, G., Felmetsger, V., Muralt, P., et al. (2012). Piezoelectric aluminum nitride thin films for micro-electromechanical systems. *MRS Bulletin, 37*(11), 1051–1061.
31. Wu, H. P., Wu, Y., Lai, Z. G., et al. (2022). A hybrid filter with extremely wide bandwidth and high selectivity using FBAR network. *IEEE Transactions on Circuits and Systems, 69*(7), 3164–3168.
32. Gu, J., Wu, Y., Lai, Z., et al. (2020). An N41-band bandpass BAW filter chip for mobile communications based on FBARs, In *Asia-Pacific Microwave Conference Proceedings*, (APMC 2020), pp 380–382.
33. Gao, Y., Zhao, K.L., Han, C., et al. (2017). Design of S-band narrowband bandpass bulk acoustic filter, In *Conference on LIDAR Imaging Detection and Target Recognition*, pp 10605.

Xiushan Wu was born in 1974. He received the Ph.D. degree in circuit and system from Southeast University, Nanjing, China, in 2009. He is currently a Professor with the School of Electrical Engineering, Zhejiang University of Water Resources and Electric Power. His main research interests include dynamic measurement and control, sensing technology, and RF-IC design.

Lin Xu was born in 1998 and holds a master's degree in electronic information from China Jiliang University. His main research interests are FBAR filter design and simulation research.

Ge Shi was born in 1982. He received the Ph.D. degree from Zhejiang University in 2018. He is currently a Professor with the China Jiliang University. He is a senior member of the China Electronics Society and IEEE Senior Member. His main research interests include IC Design, efficient environmental energy collection technology, sensor technology, detection technology, and automation devices.

Xiaowei Zhou was born in 1997 and holds a master's degree in control science and engineering from China Jiliang University. His main research interests are FBAR filter design and simulation research.

Jianping Cai was born in 1975. He received the Ph.D. degree from Zhejiang University, in 2014. He is currently a Professor with the Zhejiang University of Water Resources and Electric Power. His main research interests include nonlinear systems and adaptive control.